Article

One-Step Hydrothermal Reaction Induced Nitrogen-Doped MoS$_2$/MXene Composites with Superior Lithium-Ion Storage

Cheng Gong [1], Mengqi Long [1], Jun Xiao [1,2], Jiayi Li [1], Jun Chen [1], Yang Xiao [1], Guilai Zhang [1], Hong Gao [1,2,*] and Hao Liu [1,2,*]

[1] Joint International Laboratory on Environmental and Energy Frontier Materials, School of Environmental and Chemical Engineering, Shanghai University, Shanghai 200444, China

[2] Centre for Clean Energy Technology, Faculty of Science, University of Technology Sydney, Broadway, Sydney, NSW 2007, Australia

* Correspondence: candy1122@shu.edu.cn (H.G.); hao.liu@uts.edu.au (H.L.); Tel.: +86-21-66137488 (H.G.); +61-2-95141722 (H.L.)

Abstract: MoS$_2$, a typical transition metal dichalcogenide (TMDs), inheriting high theoretical capacity, open framework and unique electrochemical properties, is regarded as a promising electrode material. However, the low electronic conductivity and slow chemical kinetics of two-dimensional (2D) MoS$_2$ lamellars, along with the large volume expansion during cycling hinder their application in Li-ion batteries. MXene inherits the strengths of excellent metallic conductivity, a low lithium-ion diffusion potential barrier and superior mechanical stability; however, its low reversible capacity and self-stacking problems as anode still need to be solved. Herein, the MXene Ti$_3$C$_2$T$_x$ compound with MoS$_2$ through a simple one-step hydrothermal reaction is introduced. The introduction of nitrogen-doped Ti$_3$C$_2$T$_x$ can effectively restrain the volume change of MoS$_2$ and ameliorate the electronic conductivity of the whole electrode, while MoS$_2$ can alleviate the self-stacking of Ti$_3$C$_2$T$_x$ during cycling. The as-prepared MoS$_2$/MXene electrode delivers an initial discharge capacity of 1087 mA h g^{-1} with an initial Coulombic efficiency (ICE) of 81.6% at 100 mA g^{-1}, and a specific discharge capacity of 731 mA h g^{-1} can be retained after 100 cycles. The excellent electrochemical performance demonstrates that nitrogen-doped MoS$_2$/MXene can be a potential electrode material for Li-ion batteries.

Keywords: 2D materials; anode; MoS$_2$; MXene; lithium-ion batteries

1. Introduction

With the increasing energy demand, the exploration of new energy storage materials is pushing forward as well. Lithium-ion batteries (LIBs), as dominant power sources for portable electronic devices and electric/hybrid vehicles, are urgently required to develop a new generation of electrode materials to meet the growing demand. Anode materials play an important role in the practical application of lithium-ion batteries. Among the various anode materials, commercialized carbon materials have low specific capacity and poor compatibility with electrolytes, which limits their application in power battery materials, while other anode materials, including metal oxides (MOs), metal sulfides (MSs) and many other alloy-based anode materials (Sn, Si and Ti) with high specific capacities are good candidates for lithium storage [1–6].

Since the discovery of graphene in 2004, 2D materials composed of a single layer of atoms have caught significant concern. They possess unique electrical, optical as well as mechanical properties, such as high electroconductivity, good flexibility and strength, which are promising characteristics for the usage of energy storage systems. MXenes, as a new type of two-dimensional material, have attracted more and more attention as electrode material for energy storage. MXenes are 2D transition metal carbides or nitrides (M$_{n+1}$X$_n$T$_x$) deriving from ternary MAX phase (M$_{n+1}$AX$_n$) in which M represents the early transition metals (Sc,

Ti, Zr, Hf, V, Nb, Ta, Cr, Mo, etc.); A symbolizes mainly group IIIA elements; n = 1–3; X is nitrogen and/or carbon; and T_x represents the surface terminations (OH, O or F) [7]. The metallic nature of the transition metal (e.g., Ti) atoms implanted between the layers of carbon atoms endows MXenes with excellent electroconductivity [8–12]. Additionally, it is facile for polar organic molecules and metal ions to intercalate into its host structure because of the open channels provided by MXenes, thus forming composites with other materials to enhance their energy storage properties. However, their application prospects still need to be further explored due to the shortcomings of easy oxidation, low reversible capacity and self-stacking.

Transition metal dichalcogenides (TMDs) with graphene-like layer structure and excellent physicochemical properties, such as ultra-thin layer spacing, huge specific surface area, abundant edge sites, good chemical stability and adjustable forbidden band width, have drawn wide attention in the fields of optoelectronic devices, photocatalysts, energy storage and supercapacitors, etc. Compared to their metal oxide (MOs) counterparts, TMDs are expected to exhibit better mechanical stability due to their smaller volume expansion, higher initial Coulomb efficiency (ICE) and great reversibility [13–16]. Furthermore, the discharge product of MSs (Li_2S) has better electrical conductivity than that of MOs (Li_2O), and the M–S bond in MSs is weaker than the M–O bond in MOs, which may be kinetically favorable for the conversion reaction [17]. As a result, more and more attention is being focused on the design and study of the electrochemical properties of MSs. As a representative of transition metal dichalcogenides, molybdenum disulfide (MoS_2) with a layered S-Mo-S sandwich structure possesses abundant ion storage sites [18–20] and high lithium storage capacity (~670 mA h g^{-1}) [21], all of which are regarded as superior properties for energy storage application. However, the low conductivity, huge volume changes and morphology collapse of MoS_2 during electrochemical process hinder its application in practical energy storage. Interfacial modulation and combination with conductive substrates are effective strategies to optimize the electronic properties of MoS_2 [22–24]. In addition, construction MoS_2-based composite structures or introducing heteroatomic doping (N, S, P, etc.) to MoS_2 can ameliorate the chemical reaction kinetics through interlayer interactions and increase the conductivity of MoS_2 [25–28]. Chen et al. [29] synthesized 2D MoS_2-on-MXene heterostructures as anode materials for lithium-ion batteries by in situ sulfidation of $Mo_2TiC_2T_x$ MXene. As electrode for LIBs, a specific capacity of 509 mA h g^{-1} still can be realized after 100 cycles at a current density of 100 mA g^{-1}. Hu et al. [30] prepared MoS_2/MXene hybrids using freeze-drying and a subsequent thermal process. When it is the electrode for lithium-ion batteries, it remains at a capacity of 835.1 mA h g^{-1} after 110 cycles at 0.5 A g^{-1}. However, these methods require harsh reaction conditions. Moreover, the synthetic steps are not particularly concise. In addition, many enlightening works have been conducted by researchers in heteroatom doping. Xu et al. [31] fabricated series 2D MoS_2@N-doped graphene composites by a straightforward solvothermal strategy. When as the anode for sodium ion batteries, a reversible specific capacity of 141 mA h g^{-1} under 12.8 A g^{-1} can be obtained. Li et al. [32] obtained MoS_2/nitrogen-doped carbon nanorods by a polyethyleneimine (PEI)-guided hydrothermal method and subsequent calcination process. The corresponding electrode shows a reversible capacity of 397.3 mA h g^{-1} after 100 cycles at 0.1 A for sodium-ion batteries.

Based on the above experience, we generated MoS_2 in situ grown on the MXene layers (MoS_2/MXene) by using a facile hydrothermal reaction. On the one hand, the highly conductive network of the as-prepared MoS_2/MXene composite can slow down the volume expansion of MoS_2 during the cycling process, facilitate the diffusion of electrons and ions, and improves the electrochemical properties of the entire electrode. On the other hand, MoS_2 can inhibit the re-stacking of MXene, and thus the two complement each other to make up for each other's deficiencies. This synergistic effect and the nitrogen doping endow the MoS_2/MXene composite with strong mechanical stability and electrochemical properties. Meanwhile, the as-prepared stable 3D conductive network can suppress the volume change of MoS_2 during cycling. Based on all of the above advantages, excellent electrochemical performance can be anticipated. The obtained MoS_2/MXene electrode exhibit excellent

cycling stability: the initial charging/ discharging capacities of MoS_2/MXene electrode at 100 mA g^{-1} are 887 and 1087 mA h g^{-1}, respectively, with ICE of 81.6%. Meanwhile, a discharge capacity of 731 mA h g^{-1} with Coulombic efficiency of 99% can be maintained after 100 cycles.

2. Materials and Methods

The source/manufacturer of materials used in the study are shown in Table S1.

2.1. Preparation of MAX Precursor (Ti$_3$AlC$_2$)

Ti_3AlC_2 solid particles were fabricated by the molten salt technique. TiC, Ti, Al, NaCl and KCl were firstly added to the mortar in the molar ratio of 2:1:1.1:4:4 and ground for 30 min and then transferred it to a furnace calcinated at 1100 °C for 3 h in Ar atmosphere with a heating rate of 4 °C min^{-1}. The reaction products were ground for 1 h to a fine powder at room temperature, and then the residual NaCl and KCl were removed by deionized water and dried overnight (80 °C). The final MAX precursor was stored in a desiccator before use.

2.2. Preparation of MXene from MAX Precursor (f-Ti$_3$C$_2$T$_x$)

Briefly, 2 g LiF was added to 20 mL (9 M) of hydrochloric acid under stirring for 30 min, followed by the slow addition of 2 g MAX precursor. The etching process occurred in a poly tetra fluoroethylene (PTFE) reactor for 24 h at the temperature of 37 °C with a controlled speed (400 rpm) and washed with deionized water (4000 rpm, 10 min) until the pH > 6. Then, ethanol pre-infused with argon was added for ultrasonic intercalation for 1 h. The precipitate was then added to the deionized water for centrifugation, and the upper layer of solution was stored at 5 °C.

2.3. Preparation of MoS$_2$/MXene

A certain mass of MXene was dispersed in 20 mL of ethylene glycol (EG) and labeled as solution A. A certain mass (20, 60, 80, 100 mg) of $MoCl_5$ was dispersed in 20 mL of EG labeled as solution B, which was added to solution A with vigorous stirring and protected by argon gas and stirred for 24 h. Thioacetamide (TAA) with equal mass of $MoCl_5$ was added to above reaction solution and then stirred for 10 min. After that, it was transferred to Teflon-lined reactor at 160 °C for 12 h. When the reactor cooled at room temperature, the precipitate was collected by filtration. The precipitate was washed by deionized water and ethanol, and the product was dried overnight at 80 °C under vacuum. Finally, the dried samples were transferred to a tube reactor filled with argon and calcined at 220 °C for 4 h (at a heating rate of 5 °C min^{-1}). At the same time, the N element released by the decomposition of thioacetamide was doped into the MoS_2/MXene framework during the reaction. For comparison, the products with different mass ratios of $MoCl_5$ and MXene were prepared (MoS_2/MXene-x:1 (x = 2, 3, 4, 5). Note: The MoS_2/MXene-4:1 marked as (MoS_2/MXene), and the samples without MXene were also prepared (MoS_2).

2.4. Characterization

The materials synthesized in this article were studied by scanning electron microscope (SEM) and transmission electron microscope (TEM) for their microscopic morphological characteristics and elemental distribution. X-ray diffraction (XRD) was used to characterize the components and crystal structure of the materials by collecting signals with 2θ range of 3–70 ° using a Cu-Kα radiation source (wavelength 0.154 nm). The nitrogen adsorption/desorption isotherms curves and the pore-size distribution of materials were determined by means of BET tests (BET is an acronym for three scientists (Brunauer, Emmett and Teller)). Fourier transform infrared spectroscopy (FTIR) was used to qualitatively analyze the material and complement the structure of the material. X-ray photoelectron spectroscopy (XPS) analyzed the chemical valence of the material surface. Inductively

coupled plasma mass spectrometry (ICP-MS) quantified the proportion of elements in the synthesized material.

2.5. Electrochemical Measurement

The materials in this article were subsequently tested by assembling as CR 2032 button half-cells in Ar-filled glove box. The active material, acetylene black and Carboxymethyl Cellulose (CMC) were blended in deionized water at a mass ratio of 7:2:1 and applied to the copper foil and then dried under vacuum at 80 °C overnight. The average mass loading of the electrodes is about 1 mg cm^{-2}. Celgard-2400 separator was utilized to separate electrodes, and a fresh lithium sheet was applied as the counter electrode. The electrolyte was 1 M LiPF$_6$ dissolved in ethylene carbonate (EC) + diethyl carbonate (DEC) (1:1 Vol%). The voltage range was 0.01–3.0 V. The cycling and rate performance as well as Galvanostatic Intermittent Titration Technique (GITT) test were studied in the NEWARE battery test system. CHI 660E was used to test the cyclic voltammetry (CV) curve and electrochemical impedance spectroscopy (EIS) impedance analysis.

3. Results and Discussion

The schematic fabrication process of the MoS$_2$/MXene material is illustrated in Figure 1a. Firstly, the MAX phase precursor (Ti$_3$AlC$_2$) was prepared by molten salt method and chemically etching Al in Ti$_3$AlC$_2$ to prepare Ti$_3$C$_2$T$_x$ MXene nanosheets. The Ti$_3$AlC$_2$ shows typical micron-sized powders [33]. After etching treatment, the obtained MXene shows several thin flakes (Figures S1 and S2). Meanwhile, MoS$_2$/MXene composites were obtained by a typical solvothermal reaction, in which MoS$_2$ was in situ generated on the surface of MXene, and the N element released from decomposition of thioacetamide (TAA) can be doped into the MoS$_2$/MXene framework during the reaction process. Figure 1b shows the SEM image of the pristine MoS$_2$, which presents nanomicrosphere structures (100–200 nm) with tiny protrusions on the surface [34,35]. Figure 1c displays high-resolution transmission electron microscope image of the as-prepared MXene, and it can be seen that the layer spacing (d = 1.32 nm) of the few-layer MXene is identified with that previously reported work, indicating the successful synthesis of the material. Figure 1d exhibits the SEM image of the synthesized MoS$_2$/MXene. After the introduction of MXene, the MoS$_2$ nanomicrospheres were uniformly grown on the surface MXene, which offers a good transport pathway for electrons and ions. On the other hand, the layered lamellar structure of MXene wraps around MoS$_2$, which can suppress the volume expansion of MoS$_2$ during cycling process. Figure 1e–f displays the TEM image of MoS$_2$/MXene, and we can observe that MXene tightly wraps around MoS$_2$ to form a stable composite structure, and obvious folds can be observed around MoS$_2$, implying that MoS$_2$ is not simply attached to the MXene surface, and the inset selected area electron diffraction (SAED) shows obvious diffraction loops, further proving the presence of MoS$_2$. Notably, the MXene surface of the composite is not smooth compared to the pure MXene sheet, which may be due to the slight oxidation of the MXene surface. Four layers of MXene can be observed by high resolution transmission electron microscope (HRTEM) in Figure 1g, and their layer spacing (d = 1.48 nm) is increased compared to the 1.32 nm of the less-layered MXene in Figure 1d, indicating the existence of ions insert between the MXene layers during the solvothermal process, which is beneficial for lithium storage. Figure 1h–l shows mapping images of MoS$_2$/MXene. The distribution of Mo and S elements, and the surrounding uniformly distributed Ti, C and O elements correspond to MXene can be observed; meanwhile, the N element can be observed, which originates from the decomposition of thioacetamide.
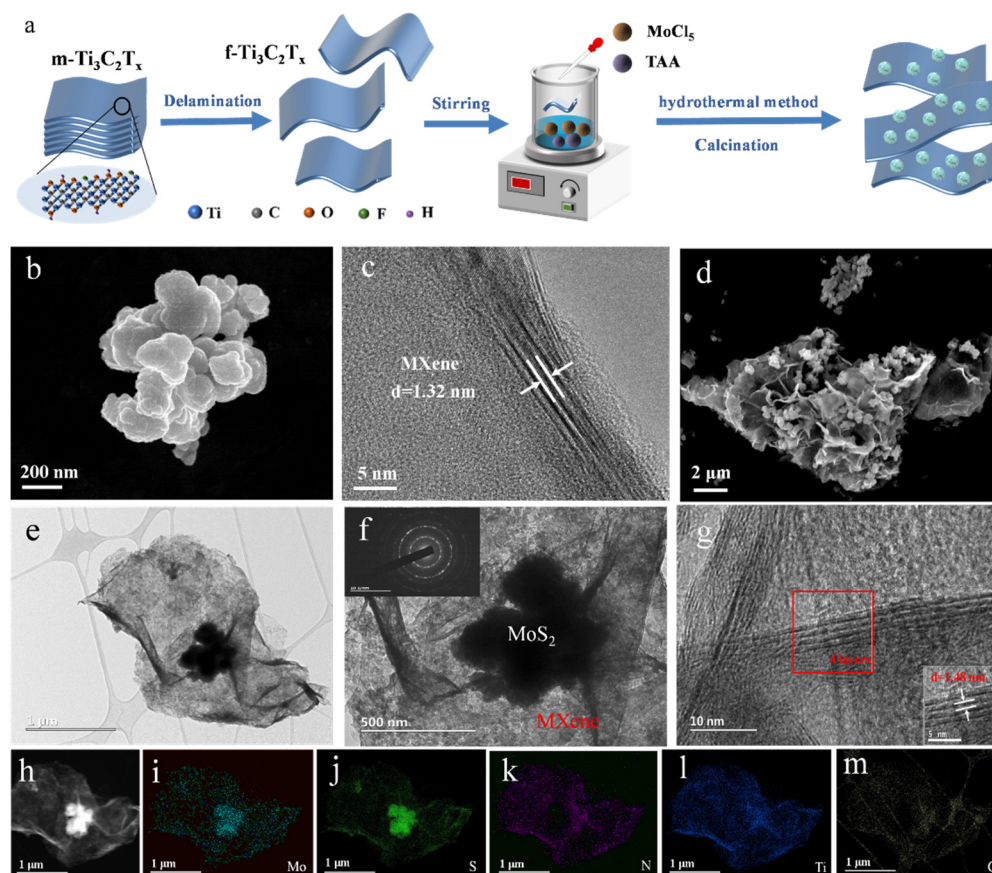
Figure 1. (**a**) Schematic diagram of the synthesis process of MoS_2/MXene. (**b**) SEM images of MoS_2; (**c**) HRTEM images of MXene; (**d**) SEM images of MoS_2/MXene; (**e–f**) TEM images of MoS_2/MXene, where inset (**f**) is SEAD pattern of MoS_2/MXene; (**g**) HRTEM images of MXene in the MoS_2/MXene composite, where inset is its HRTEM image at higher magnification; (**h–m**) elemental mapping of MoS_2/MXene.

Figure 2a illustrates the XRD plots of MoS_2/MXene composites with different ratios, showing that the different MoS_2 content does not significantly affect the XRD, and the (003) crystal plane of MoS_2 at 14.4° is still retained. In addition, the (002) crystallographic plane of MXene in the composite is biased to a smaller angle, indicating an increase in the MXene layer spacing, which is identified with the TEM plots. Notably, the peak at around $2\theta = 25°$ corresponds to TiO_2, indicating a slight oxidation of MXene during the hydrothermal reaction. Meanwhile, the synthesized MAX and MoS_2 are identified with the standard card, indicating the successful synthesis of them, and the (002) plane of the prepared MXene is shifted from 9.38° to a smaller 6.52° after etching, implying an expanded layer spacing (d = 1.36 nm) for the layered MXene calculated by the Bragg equation, which matches the HRTEM image in Figure 1c (Figures S3 and S4). Figures S5 and 2b show Raman spectra of the MXene, MoS_2 and MoS_2/MXene composites. As for the Raman spectrum of MXene (Figure S5), the region between 230 and 470 cm^{-1} indicates the in-plane (E_g) vibrations of the surface groups attached to the titanium atoms; the region between 580 and 730 cm^{-1} can be assigned mainly to carbon vibrations (E_g and A_{1g}), which further confirms the successful etching of MXene. As for MoS_2 and MoS_2/MXene composites (Figure 2b), two typical peaks at around 400 cm^{-1} belong to the E_{12g} and A_{1g} vibrational modes of MoS_2 [36]. The distinct D band and G band can be observed around 1350 cm^{-1} and 1550 cm^{-1}, which belong to the defects of the carbon-based material and the vibrations of the sp^2 hybridized carbon atoms, respectively. Clear shifts can be detected of the D band and G band of the MoS_2/MXene composites towards the higher energy regions, demonstrating the recovery of the conjugate structure after the nitrogen atoms incorporated into the lattice of MXene [37]. In addition,

the intensity ratios (I_D/I_G) of MoS_2 and MoS_2/MXene are 0.86 and 0.92, respectively, suggesting the existence of a great number of defects and vacancies in the MoS_2/MXene material, which facilitates the lithium-ion diffusion and also provides sufficient space for the storage of lithium ions. The FTIR spectra of MXene/MoS_2 are presented in Figure S6, the peaks near 580 cm^{-1} and 1100 cm^{-1} could be assigned to the stretching vibrations of Ti–C and C–O bonds, respectively, caused by the characteristic structure of Ti_3C_2. In addition, the peaks at 700–900 cm^{-1} are attributed to the Ti–O–Mo bond. Additionally, the peak near 615 cm^{-1} corresponds to the vibrational absorption peak of the S–S bond of MoS_2. It can be concluded that MoS_2 behaves in a strong interaction with MXene and realizes stable constructions of the as-prepared MXene/MoS_2 composite. Furthermore, the chemical valence state of the MoS_2/MXene material surface was investigated by means of XPS. From the full spectrum (Figure 2c), the elements of O, Ti, Mo, C and S elements can be detected, and trace amounts of N elements are also observed. Additionally, as shown in Figure S7a, F, O, Ti, C and Cl are clearly detected in the XPS spectrum of MXene. The presence of Cl may come from the molten salt process. Furthermore, in the high-resolution Mo 3d spectrum of MXene/MoS_2 composite (Figure 2d), two distinct peaks in pure MoS_2 at 229.1 eV (Mo 3d$_{5/2}$) and 232.2 eV (Mo 3d$_{3/2}$) can be ascribed to Mo^{4+}. In addition, the peak near 235.5 eV is attributed to Mo^{6+} (oxidation of the MoS_2 surface). The peak at 226.3 eV is attributed to the Mo–S bond. Correspondingly, in the MoS_2/MXene composite, in addition to the four peaks mentioned above, the peaks at 230.4 and 233.3 eV are ascribed to Mo 3d$_{5/2}$ and Mo 3d$_{3/2}$, respectively, suggesting that Mo–S–C and Mo–O–C bonds are formed. These bonds enhance the interaction of MoS_2 and MXene and enhance the structural stability of the material during cycling. The high-resolution spectrum of Ti 2p in Figure 2e contains peaks associated with Ti–O (sp^1), Ti^{2+} (2p$^{1/2}$), Ti–C, Ti–O (sp^3), Ti–N and Ti–S. And it is noteworthy that the two peaks at 456.7 and 455.6 eV correspond to Ti–N and Ti–S bonds, respectively [38,39], indicating that MoS_2 is firmly anchored to the surface of MXene through the Ti-S bond, which strengthens the structural stability of the material. Additionally, the presence of Ti–N bonds indicates the successful doping of N elements. The peaks at 533.6, 532.1 and 530.4 eV in the O 1s high-resolution spectrum (Figure 2f) are attributed to C–Ti–(OH)$_x$, C–Ti/Mo–O$_x$ and Ti–O bonds, respectively. The N 1s high-resolution spectrum in Figure 2g has four peaks. The peaks at 397.2 and 399.8 eV are attributed to pyridine nitrogen and pyrrole nitrogen, respectively, and the strong peak at 395.1 eV is attributed to Mo 3p$_{3/2}$. The peak at 396.1 eV corresponds to the Ti–N bond, which coincides with the Ti 2p fine spectrum, and nitrogen doping can improve the electrochemical performance of the material [40]. In addition, the atomic percentages of the individual elemental content of the materials analyzed by XPS data are shown in Table S2. The masses of Mo, S and Ti elements in the synthesized materials were also quantified by ICP-MS (Table S3). Meanwhile, the MoS_2/MXene displays a specific surface area of 41.67 m^2 g^{-1} and pore size mainly distributed between 2 and 5 nm (Figure S8). The large specific surface area combined with rich mesopores facilitates the ion transportation and electrolyte diffusion.

The electrochemical performance was evaluated by a half-cell system. Figure 3a illustrates the CV curves of MoS_2/MXene in the first three cycles at 0.1 mV s^{-1} scanning rate and in a voltage range of 0.01 to 3.0 V (vs. Li$^+$/Li) for the study of the lithium ion lithiation/de-lithiation behavior. Within the initial cathodic scan curve, the peaks at 0.5–1.0 V are attributed to the formation of Li$_x$MoS$_2$ in the Li$^+$ intercalated into the MoS_2 and Li$^+$ intercalated into the MXene interlayer to form Li$_y$Ti$_3$C$_2$T$_x$, along with the generation of solid electrolyte interphase (SEI) film, and the peak at around 1.9 V is probably attributed to the reduction of Li$_x$MoS$_2$ to Mo and Li$_2$S. The reduction peak at 0.01 V is attributed to the electrochemical decomposition of MoS_2, resulting in the intercalation of Mo metal into Li$_2$S. Within the initial anodic scan curve, the peak around 1.6 V is attributed to the oxidation of Mo and the de-intercalating of Li$^+$ between MXene layers, while the peak at ~2.3 V relates to the de-lithiating of Li$_2$S [41]. In the two subsequent cycles, the

CV curves nearly overlap, suggesting a stable structure of the electrode. The relevant electrochemical reaction equations are shown in equations as follows:
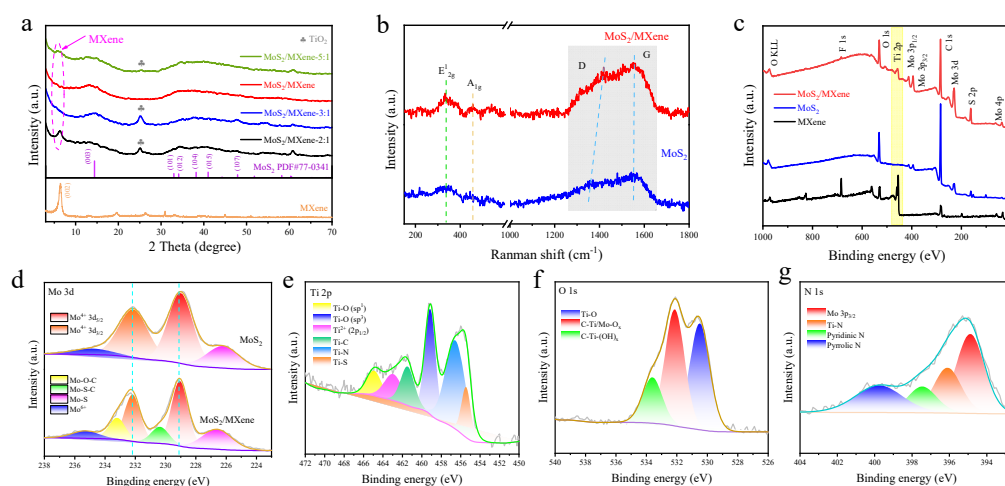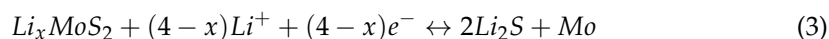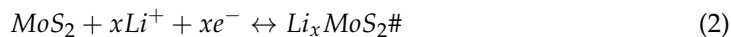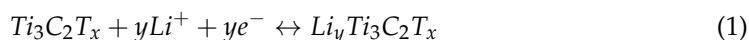
$$Ti_3C_2T_x + yLi^+ + ye^- \leftrightarrow Li_yTi_3C_2T_x \tag{1}$$

$$MoS_2 + xLi^+ + xe^- \leftrightarrow Li_xMoS_2\# \tag{2}$$

$$Li_xMoS_2 + (4-x)Li^+ + (4-x)e^- \leftrightarrow 2Li_2S + Mo \tag{3}$$

Figure 2. (**a**) XRD patterns of MoS_2/MXene$-$x:1 (x = 2, 3, 4, 5) and MXene; (**b**) Raman spectra of MoS_2/MXene composites and MoS_2; (**c**) XPS full spectra of MoS_2/MXene, MoS_2 and MXene; high-resolution (**d**) Mo 3d XPS spectra of MoS_2 and MoS_2/MXene; high-resolution (**e**) Ti 2p (**f**) O 1s and (**g**) N 1s XPS spectra of MoS_2/MXene.
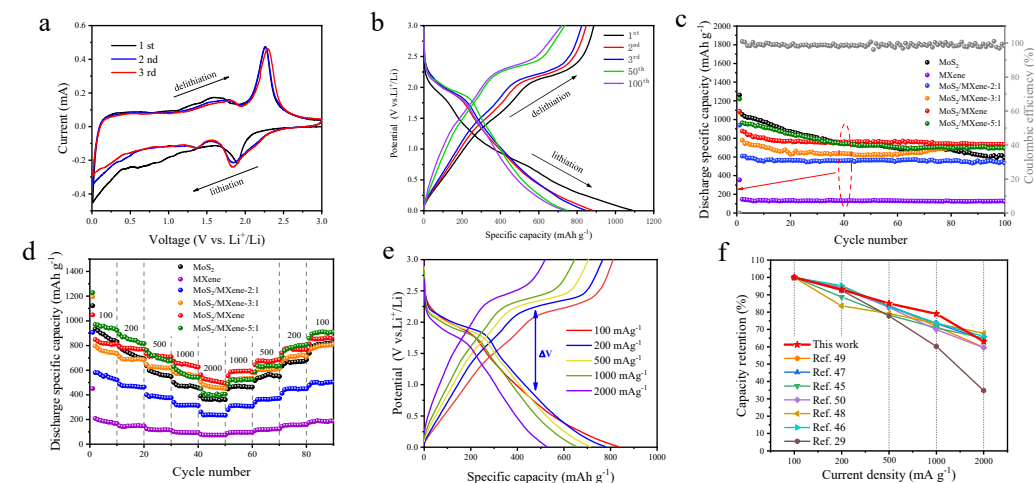

Figure 3. (**a**) CV curves of MoS_2/MXene at the scan rate of 0.1 mV s^{-1}; (**b**) charge/discharge profiles of MoS_2/MXene at 100 mA g^{-1}; (**c**) cycling performance of MoS_2, MXene and MoS_2/MXene$-$x:1 (x = 2, 3, 4, 5) at 100 mA g^{-1}; (**d**) rate performance of MoS_2, MXene and MoS_2/MXene$-$x:1 (x = 2, 3, 4, 5) at different current densities (100, 200, 500, 1000 and 2000 mA g^{-1}); (**e**) charge/discharge profiles of MoS_2/MXene electrode at different current densities; (**f**) comparison of the capacity retention of as-prepared MoS_2/MXene with other related materials.

The corresponding charge/discharge profiles for different cycle times at 100 mA g^{-1} are illustrated in Figure 3b. The plateaus of 1.37 and 1.8 V for the discharge process relate to the formation of Li_xMoS_2 and Li_2S, while the plateaus of 1.6 and 2.3 V for the charging process are equivalent to the oxidation of Mo or the de-lithiation of $Li_yTi_3C_2T_x$ and Li_2S, which is in line with the results of the CV curves. The initial Coulombic efficiency

(ICE) of the material was calculated to be 81.60%, which was far superior to pure MoS_2 and MXene, followed by a Coulombic efficiency of 96.24% in the second cycle, and it was able to maintain a high Coulombic efficiency in the subsequent cycles (98.99% at 50 cycles and 99.36% at 100 cycles). In addition, the composite has a low capacity decay rate and good cycling performance with charge/discharge capacities of 719/731 mA h g^{-1}, respectively, after 100 cycles. The lower Coulombic efficiency in the first cycle may be due to irreversible capacity decay and the decomposition of electrolytes for SEI. The cycling performance of the MoS_2/MXene electrode and the counterparts with different MoS_2 and MXene ratios at 100 mA g^{-1} was investigated (Figure 3c). It can be found that the MXene with unique structure delivers a very stable cycling performance (maintaining 94% capacity retention compared to the third cycle after 100 cycles). Pure MoS_2 electrode behaves with a first discharge capacity of 1261 mA h g^{-1}, but the discharge capacity drops to 588 mA h g^{-1} after 100 cycles. This could be attributed to the structural collapse caused by the volume expansion during the charging and discharging process. When incorporating with MXene, the volume expansion problem can be alleviated, and thus the cycling stability can be enhanced. All electrodes show capacity decay in the first 20 cycles, which could be due to the formation of SEI film. Among different compositions, the MoS_2/MXene electrode behaves the best cycling stability, retaining a discharge capacity of 731 mA h g^{-1} after 100 cycles and having a Coulombic efficiency of approximately 99%. In comparison, the MoS_2/MXene-2:1, MoS_2/MXene-3:1 and MoS_2/MXene-5:1 electrodes retain reversible capacities of 534 mA h g^{-1}, 704 mA h g^{-1} and 691 mA h g^{-1}, respectively. For the MoS_2/MXene-2:1 and MoS_2/MXene-3:1 electrodes, the cycling stability of the materials was improved compared to the pristine MoS_2, but the capacities were lower due to the large proportion of MXene content, while the capacity decay was more serious for MoS_2/MXene-5:1, probably due to the high MoS_2 content, meaning the active material would accumulate and agglomerate on the MXene surface. By the above comparison, the electrode MoS_2/MXene with the ratio of 4:1 behaves with the most excellent electrochemical properties. Moreover, the electrochemical properties of the MXene was studied (Figure S9), and it delivers a first discharge capacity of 355 mA h g^{-1} with initial Coulombic efficiency of only 40%. Additionally, the rate performance of these electrodes was also investigated at different current densities (Figure 3d). The capacity of MoS_2/MXene at current densities of 100, 200, 500, 1000 and 2000 mA g^{-1} were 834 mA h g^{-1} (3rd cycle), 778 mA h g^{-1} (13th cycle), 713 mA h g^{-1} (23rd cycle), 655 mA h g^{-1} (33rd cycle) and 526 mA h g^{-1} (43rd cycle), respectively, and when the current density backed to 100 mA g^{-1} again, the capacity could be retained at 852 mA h g^{-1} (83rd cycle). Clearly, the capacities of the MoS_2/MXene-2:1 and MoS_2/MXene-3:1 electrodes at different current densities were higher than those of pure MoS_2 electrode under the same conditions. For MoS_2/MXene-5:1, although the reversible capacity increases, the rate performance decreased due to the aggregation and destruction of the composite structure during cycling, which is also consistent with the cycling performance results. The charge/discharge profiles of MoS_2/MXene electrode at the corresponding number of cycles are shown in Figure 3e. As can be seen, although the overpotential (ΔV) increases with the current density, it still retains a clear charge/discharge plateau, indicating an excellent rate performance. However, at high current densities, ion diffusion and electron transfer become slower due to the slow redox reaction resulting from the generation of the concentration polarization [42–44]. The capacity values of different materials at the 3rd, 13th, 23rd, 43rd, 53rd, 63rd, 73rd and 83rd cycles are listed in Table S4. In addition, the electrochemical performances of previously reported MoS_2-based electrodes are summarized in comparison with the MoS_2/MXene electrode in this work (Figure 3f) [29,45–50]. It can be seen that at different current densities the capacity retention of this work is at a relatively high level.

In order to comprehensively understand the synergistic effect between MoS_2 and MXene, we drew a schematic diagram comparing the lithiation and de-lithiation processes of the MoS_2, MXene and MoS_2/MXene anode materials. As shown in Figure 4a, the pure MXene lamellar material undergoes different degrees of re-stacking during the

lithiation process, which reduces the layer spacing and negatively affect the ion transport in the lamellar material. While the pure MoS_2 lamellar material undergoes irreversible volume expansion during the lithiation process, which also degrades the electrochemical performance of the material, the above two materials have undergone different degrees of volume changes during the lithiation process, leading to irreversible phenomenon during the de-lithiation process. The MoS_2/MXene composite obtained by one-step hydrothermal method solves the above problems well. On the one hand, the existence of MXene slows down the volume expansion of MoS_2 during cycling, and on the other hand, MoS_2 can alleviate the restacking of MXene. The MoS_2 and MXene complement each other and make up for each other's shortcomings. We also studied the EIS and the GITT of the electrodes to better elucidate the transfer kinetics of the electrodes. Figure 4b displays the Nyquist plot obtained from the EIS test. The plot consists of two parts, a semicircle in high-frequency region and a diagonal line in low-frequency region, belonging to the charge transfer resistance R_{ct} and the diffusion-related Warburg impedance (Z_w), respectively, which indicates that the electrochemical behavior is controlled by charge transfer and ion diffusion [51]. We can find that MoS_2 displays the largest R_{ct} and MXene shows the smallest R_{ct}. There is no significant difference in the R_{ct} (after one cycle) of the MoS_2/MXene-2:1, MoS_2/MXene-3:1, MoS_2/MXene and MoS_2/MXene-5:1 electrodes, but the slope in the low frequency region shows that the MoS_2/MXene electrode has the smallest Z_w. The EIS analysis shows that the introduction of MXene reduces the impedance of electron diffusion and improves the electrical conductivity of the material. Moreover, it is found that the sample MoS_2/MXene has the lowest R_{ct} and Z_w, which also corresponds to the previous electrochemical performance. The Li^+ diffusion coefficient (D_{Li}^+) was calculated based on the results of the constant GITT and the detailed calculation process is presented in the Supporting Information. The test was carried out by applying a current pulse of 50 mA g^{-1} for 30 min with a chirality time of 30 min. The results of the test are given in Figure 4c–d, and the D_{GITT} of MoS_2/MXene is higher in the first discharge platform than in the second one because the first discharge platform belongs to the embedding of protons and the second one links with the embedding of lithium ions, a phenomenon attributed to the diffusion coefficient of lithium ions itself is lower than that of protons, and the charging platform also exhibits a similar pattern [52–54]. After comparison, it was found that the time required to perform a charge/discharge cycle for MoS_2/MXene was shorter than that of the MoS_2, indicating a more rapid embedding/disembedding process of lithium ions. By comparing the calculated D_{Li}^+, the results represent the energy barrier for Li^+ diffusion. Apparently, the average D_{Li}^+ of MoS_2/MXene is larger than MoS_2, and it can be seen that MoS_2 is nearly half an order of magnitude lower than MoS_2/MXene; meanwhile, both have similar variation patterns, further indicating their excellent diffusion kinetic behavior. By the above EIS and GITT analysis, the introduction of MXene lamellar can provide sufficient surface electron mobility and efficient ion transport to promote electrochemical kinetic behavior.
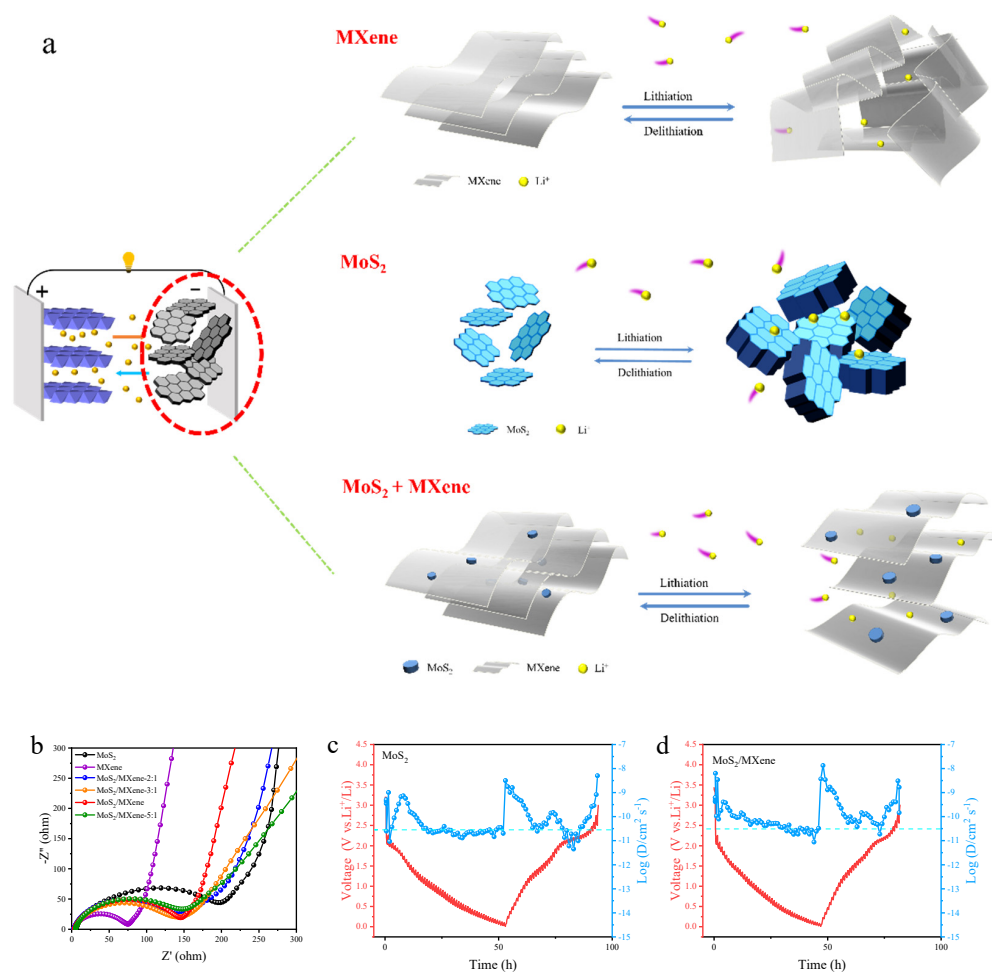
Figure 4. (**a**) Schematic diagram of the processes of lithiation and de-lithiation in MXene, MoS_2 and MXene/MoS_2; (**b**) Nyquist plots of MoS_2, MXene, MoS_2/MXene$-$2:1, MoS_2/MXene$-$3:1, MoS_2/MXene and MoS_2/MXene$-$5:1 after the first charge/discharge cycle; GITT results of (**c**) MoS_2 and (**d**) MoS_2/MXene.

4. Conclusions

In summary, the MoS_2/MXene-x:1 (x = 2, 3, 4, 5) composites were prepared via a facile hydrothermal strategy and applied to the corresponding electrode for lithium-ion batteries. It was demonstrated by Raman, XRD and XPS that the synthesized MoS_2 formed a strong combination with the MXene through the Ti–S and Ti–O–Mo bonds; meanwhile, the N element derived from the decomposition of thioacetamide was incorporated into the composite to enhance the electrochemical properties. As expected, the corresponding MoS_2/MXene electrode delivers initial charge/discharge capacities of 887/1087 mA h g^{-1}, respectively, at 100 mA g^{-1} with an ICE of 81.6%, and a discharge capacity of 731 mA h g^{-1} can be retained after 100 cycles. Furthermore, the EIS and GITT investigations demonstrate that the introduction of MXene is beneficial to improve electronic conductivity, boost reaction kinetics and enhance stability. Additionally, the nitrogen-doped $Ti_3C_2T_x$ can effectively suppress the volume change of MoS_2 and further enhance the electrical conductivity of the entire electrode, whereas MoS_2 can reduce the self-stacking of $Ti_3C_2T_x$. These excellent results demonstrate the promising potential of the MoS_2/MXene electrode for energy storage systems.

References

1. Huang, T.; Long, M.; Xiao, J.; Liu, H.; Wang, G. Recent research on emerging organic electrode materials for energy storage. *Energy Mater.* **2021**, *1*, 09. [CrossRef]
2. Jun, X.; Xiao, L.; Kaikai, T.; Mengqi, L.; Jun, C.; Dandan, W.; Hong, G.; Hao, L. Enhanced electrochemical performance of Li-rich cathode material for lithium-ion batteries. *Surf. Innov.* **2022**, *10*, 119–127.
3. Lu, J.; Chen, Z.W.; Pan, F.; Cui, Y.; Amine, K. High-Performance Anode Materials for Rechargeable Lithium-Ion Batteries. *Electrochem. Energy Rev.* **2018**, *1*, 35–53. [CrossRef]
4. Nitta, N.; Wu, F.X.; Lee, J.T.; Yushin, G. Li-ion battery materials: Present and future. *Mater. Today* **2015**, *18*, 252–264. [CrossRef]
5. Pramanik, A.; Chattopadhyay, S.; De, G.; Mahanty, S. Efficient energy storage in mustard husk derived porous spherical carbon nanostructures. *Mater. Adv.* **2021**, *2*, 7463–7472. [CrossRef]
6. Pramanik, A.; Maiti, S.; Sreemany, M.; Mahanty, S. Rock-Salt-Templated Mn$_3$O$_4$ Nanoparticles Encapsulated in a Mesoporous 2D Carbon Matrix: A High Rate 2 V Anode for Lithium-Ion Batteries with Extraordinary Cycling Stability. *Chemistryselect* **2017**, *2*, 7854–7864. [CrossRef]
7. Anasori, B.; Lukatskaya, M.R.; Gogotsi, Y. 2D metal carbides and nitrides (MXenes) for energy storage. *Nat. Rev. Mater.* **2017**, *2*, 98. [CrossRef]
8. Enyashin, A.N.; Ivanoyskii, A.L. Structural and Electronic Properties and Stability of MXenes Ti$_2$C and Ti$_3$C$_2$ Functionalized by Methoxy Groups. *J. Phys. Chem. C* **2013**, *117*, 13637–13643. [CrossRef]
9. Han, M.K.; Yin, X.W.; Wu, H.; Hou, Z.X.; Song, C.Q.; Li, X.L.; Zhang, L.T.; Cheng, L.F. Ti$_3$C$_2$ MXenes with Modified Surface for High-Performance Electromagnetic Absorption and Shielding in the X-Band. *ACS Appl. Mater. Interfaces* **2016**, *8*, 21011–21019. [CrossRef]
10. Karlsson, L.H.; Birch, J.; Halim, J.; Barsoum, M.W.; Persson, P.O.A. Atomically Resolved Structural and Chemical Investigation of Single MXene Sheets. *Nano Lett.* **2015**, *15*, 4955–4960. [CrossRef]
11. Lipatov, A.; Alhabeb, M.; Lukatskaya, M.R.; Boson, A.; Gogotsi, Y.; Sinitskii, A. Effect of Synthesis on Quality, Electronic Properties and Environmental Stability of Individual Monolayer Ti$_3$C$_2$ MXene Flakes. *Adv. Electron. Mater.* **2016**, *2*, 00255.
12. Guo, X.; Gao, H.; Wang, S.; Yang, G.; Zhang, X.; Zhang, J.; Liu, H.; Wang, G. MXene-Based Aerogel Anchored with Antimony Single Atoms and Quantum Dots for High-Performance Potassium-Ion Batteries. *Nano Lett.* **2022**, *22*, 1225–1232. [CrossRef]
13. Gao, H.; Zhou, T.F.; Zheng, Y.; Zhang, Q.; Liu, Y.Q.; Chen, J.; Liu, H.K.; Guo, Z.P. CoS Quantum Dot Nanoclusters for High-Energy Potassium-Ion Batteries. *Adv. Funct. Mater.* **2017**, *27*, 02634. [CrossRef]
14. Wang, Y.K.; Liu, M.C.; Cao, J.Y.; Zhang, H.J.; Kong, L.B.; Trudgeon, D.P.; Li, X.H.; Walsh, F.C. 3D Hierarchically Structured CoS Nanosheets: Li$^+$ Storage Mechanism and Application of the High-Performance Lithium-Ion Capacitors. *ACS Appl. Mater. Interfaces* **2020**, *12*, 3709–3718. [CrossRef]
15. Zhang, S.L.; Ying, H.J.; Huang, P.F.; Wang, J.L.; Zhang, Z.; Yang, T.T.; Han, W.Q. Rational Design of Pillared SnS/Ti$_3$C$_2$T$_x$ MXene for Superior Lithium-Ion Storage. *ACS Nano* **2020**, *14*, 17665–17674. [CrossRef]
16. Zhang, X.Y.; Shi, H.T.; Liu, L.S.; Min, C.Y.; Liang, S.T.; Xu, Z.W.; Xue, Y.L.; Hong, C.X.; Cai, Z.J. Construction of MoS$_2$/Mxene heterostructure on stress-modulated kapok fiber for high-rate sodium-ion batteries. *J. Colloid Interface Sci.* **2022**, *605*, 472–482. [CrossRef] [PubMed]
17. Xiao, Y.; Lee, S.H.; Sun, Y.K. The Application of Metal Sulfides in Sodium Ion Batteries. *Adv. Energy Mater.* **2017**, *7*, 01329. [CrossRef]

18. Liu, C.; Wang, Y.; Sun, J.; Chen, A. A Review on Applications of Layered Phosphorus in Energy Storage. *Trans. Tianjin Univ.* **2020**, *26*, 104–126. [CrossRef]

19. Su, F.; Hou, X.C.; Qin, J.Q.; Wu, Z.S. Recent Advances and Challenges of Two-Dimensional Materials for High-Energy and High-Power Lithium-Ion Capacitors. *Batteries Supercaps* **2020**, *3*, 10–29. [CrossRef]

20. Wang, L.L.; Zhang, Q.F.; Zhu, J.Y.; Duan, X.D.; Xu, Z.; Liu, Y.T.; Yang, H.G.; Lu, B.A. Nature of extra capacity in MoS_2 electrodes: Molybdenum atoms accommodate with lithium. *Energy Storage Mater.* **2019**, *16*, 37–45. [CrossRef]

21. Ding, S.J.; Zhang, D.Y.; Chen, J.S.; Lou, X.W. Facile synthesis of hierarchical MoS_2 microspheres composed of few-layered nanosheets and their lithium storage properties. *Nanoscale* **2012**, *4*, 95–98. [CrossRef] [PubMed]

22. Wu, X.H.; Wang, Z.Y.; Yu, M.Z.; Xiu, L.Y.; Qiu, J.S. Stabilizing the MXenes by Carbon Nanoplating for Developing Hierarchical Nanohybrids with Efficient Lithium Storage and Hydrogen Evolution Capability. *Adv. Mater.* **2017**, *29*, 07017. [CrossRef] [PubMed]

23. Yuan, Z.Y.; Wang, L.L.; Li, D.D.; Cao, J.M.; Han, W. Carbon-Reinforced Nb_2CT_x MXene/MoS_2 Nanosheets as a Superior Rate and High-Capacity Anode for Sodium-Ion Batteries. *ACS Nano* **2021**, *15*, 7439–7450. [CrossRef]

24. Zhang, Y.L.; Mu, Z.J.; Yang, C.; Xu, Z.K.; Zhang, S.; Zhang, X.Y.; Li, Y.J.; Lai, J.P.; Sun, Z.H.; Yang, Y.; et al. Rational Design of MXene/1T-2H MoS_2-C Nanohybrids for High-Performance Lithium-Sulfur Batteries. *Adv. Funct. Mater.* **2018**, *28*, 07578. [CrossRef]

25. Chen, Y.L.; Su, F.Y.; Xie, H.Q.; Wang, R.P.; Ding, C.H.; Huang, J.D.; Xu, Y.X.; Ye, L.Q. One-step construction of S-scheme heterojunctions of N-doped MoS_2 and S-doped g-C_3N_4 for enhanced photocatalytic hydrogen evolution. *Chem. Eng. J.* **2021**, *404*, 126498. [CrossRef]

26. Han, J.H.; Zhang, S.C.; Song, Q.G.; Yan, H.Y.; Kang, J.H.; Guo, Y.R.; Liu, Z.F. The synergistic effect with S-vacancies and built-in electric field on a TiO_2/MoS_2 photoanode for enhanced photoelectrochemical performance. *Sustain. Energ. Fuels* **2021**, *5*, 509–517. [CrossRef]

27. Nguyen, D.C.; Tran, D.T.; Doan, T.L.L.; Kim, D.H.; Kim, N.H.; Lee, J.H. Rational Design of Core@shell Structured CoS_x@Cu_2MoS_4 Hybridized MoS_2/N,S-Codoped Graphene as Advanced Electrocatalyst for Water Splitting and Zn-Air Battery. *Adv. Energy Mater.* **2020**, *10*, 03289. [CrossRef]

28. Xie, D.; Xia, X.H.; Wang, Y.D.; Wang, D.H.; Zhong, Y.; Tang, W.J.; Wang, X.L.; Tu, J.P. Nitrogen-Doped Carbon Embedded MoS_2 Microspheres as Advanced Anodes for Lithium- and Sodium-Ion Batteries. *Chem.-Eur. J.* **2016**, *22*, 11617–11623. [CrossRef]

29. Chen, C.; Xie, X.; Anasori, B.; Sarycheva, A.; Makaryan, T.; Zhao, M.; Urbankowski, P.; Miao, L.; Jiang, J.; Gogotsi, Y. MoS_2-on-MXene Heterostructures as Highly Reversible Anode Materials for Lithium-Ion Batteries. *Angew. Chem.-Int. Edit.* **2018**, *57*, 1846–1850. [CrossRef]

30. Hu, Z.; Kuai, X.; Chen, J.; Sun, P.; Zhang, Q.; Wu, H.-H.; Zhang, L. Strongly Coupled MoS_2 Nanocrystal/Ti_3C_2 Nanosheet Hybrids Enable High-Capacity Lithium-Ion Storage. *ChemSusChem* **2020**, *13*, 1485–1490. [CrossRef]

31. Xu, X.; Zhao, R.S.; Ai, W.; Chen, B.; Du, H.F.; Wu, L.S.; Zhang, H.; Huang, W.; Yu, T. Controllable Design of MoS_2 Nanosheets Anchored on Nitrogen-Doped Graphene: Toward Fast Sodium Storage by Tunable Pseudocapacitance. *Adv. Mater.* **2018**, *30*, 1800658. [CrossRef]

32. Li, J.B.; Tang, S.C.; Li, Z.Q.; Wang, C.Y.; Li, J.L.; Li, X.D.; Ding, Z.B.; Pan, L.K. Crosslinking Nanoarchitectonics of Nitrogen-doped Carbon/MoS_2 Nanosheets/$Ti_3C_2T_x$ MXene Hybrids for Highly Reversible Sodium Storage. *ChemSusChem* **2021**, *14*, 5293–5303. [CrossRef] [PubMed]

33. Li, M.; Lu, J.; Luo, K.; Li, Y.B.; Chang, K.K.; Chen, K.; Zhou, J.; Rosen, J.; Hultman, L.; Eklund, P.; et al. Element Replacement Approach by Reaction with Lewis Acidic Molten Salts to Synthesize Nanolaminated MAX Phases and MXenes. *J. Am. Chem. Soc.* **2019**, *141*, 4730–4737. [CrossRef] [PubMed]

34. Lin, W.J.; Huang, Y.H.; He, G.Q. Unique CoS hierarchitectures for high-performance lithium ion batteries. *Crystengcomm* **2018**, *20*, 6727–6732. [CrossRef]

35. Zhou, Y.P.; Li, J.; Yang, Y.; Luo, B.; Zhang, X.; Fong, E.L.E.; Chu, W.; Huang, K.M. Unique 3D flower-on-sheet nanostructure of NiCo LDHs: Controllable microwave-assisted synthesis and its application for advanced supercapacitors. *J. Alloy. Compd.* **2019**, *788*, 1029–1036. [CrossRef]

36. Li, C.R.; Song, H.; Mao, C.M.; Peng, H.R.; Li, G.C. A novel MoS_2 nanosheets-decorated Sb@Sb_2S_3@C tubular composites as anode material for high performance lithium ion battery. *J. Alloy. Compd.* **2019**, *786*, 169–176. [CrossRef]

37. Yu, J.L.; Zeng, M.L.; Zhou, J.; Chen, H.D.; Cong, G.T.; Liu, H.C.; Ji, M.W.; Zhu, C.Z.; Xu, J. A one-pot synthesis of nitrogen doped porous MXene/TiO_2 heterogeneous film for high-performance flexible energy storage. *Chem. Eng. J.* **2021**, *426*, 130765. [CrossRef]

38. Luo, J.M.; Zheng, J.H.; Nai, J.W.; Jin, C.B.; Yuan, H.D.; Sheng, O.W.; Liu, Y.J.; Fang, R.Y.; Zhang, W.K.; Huang, H.; et al. Atomic Sulfur Covalently Engineered Interlayers of Ti_3C_2 MXene for Ultra-Fast Sodium-Ion Storage by Enhanced Pseudocapacitance. *Adv. Funct. Mater.* **2019**, *29*, 08107. [CrossRef]

39. Wang, Z.; Li, X.Y.; Xuan, C.X.; Li, J.J.; Jiang, Y.L.; Xiao, J.R. Photo-synergetic nitrogen-doped MXene/reduced graphene oxide sandwich-like architecture for high-performance lithium-sulfur batteries. *Int. J. Energy Res.* **2021**, *45*, 2728–2738. [CrossRef]

40. Ye, Z.Q.; Jiang, Y.; Li, L.; Wu, F.; Chen, R.J. Self-Assembly of 0D-2D Heterostructure Electrocatalyst from MOF and MXene for Boosted Lithium Polysulfide Conversion Reaction. *Adv. Mater.* **2021**, *33*, 2101204. [CrossRef]

41. He, F.Y.; Tang, C.; Liva, Y.D.; Li, H.T.; Du, A.J.; Zhang, H.J. Carbon-coated MoS_2 nanosheets@CNTs-Ti_3C_2 MXene quaternary composite with the superior rate performance for sodium-ion batteries. *J. Mater. Sci. Technol.* **2022**, *100*, 101–109. [CrossRef]

42. Bao, W.Z.; Shuck, C.E.; Zhang, W.X.; Guo, X.; Gogotsi, Y.; Wang, G.X. Boosting Performance of Na-S Batteries Using Sulfur-Doped Ti$_3$C$_2$T$_x$ MXene Nanosheets with a Strong Affinity to Sodium Polysulfides. *ACS Nano* **2019**, *13*, 11500–11509. [CrossRef] [PubMed]

43. Dong, Y.F.; Zheng, S.H.; Qin, J.Q.; Zhao, X.J.; Shi, H.D.; Wang, X.H.; Chen, J.; Wu, Z.S. All-MXene-Based Integrated Electrode Constructed by Ti$_3$C$_2$ Nanoribbon Framework Host and Nanosheet Interlayer for High-Energy-Density Li-S Batteries. *ACS Nano* **2018**, *12*, 2381–2388. [CrossRef] [PubMed]

44. Mou, J.R.; Li, Y.J.; Liu, T.; Zhang, W.J.; Li, M.; Xu, Y.T.; Zhong, L.; Pan, W.H.; Yang, C.H.; Huang, J.L.; et al. Metal-Organic Frameworks-Derived Nitrogen-Doped Porous Carbon Nanocubes with Embedded Co Nanoparticles as Efficient Sulfur Immobilizers for Room Temperature Sodium-Sulfur Batteries. *Small Methods* **2021**, *5*, 00455. [CrossRef] [PubMed]

45. Bai, J.; Zhao, B.C.; Zhou, J.F.; Si, J.G.; Fang, Z.T.; Li, K.Z.; Ma, H.Y.; Dai, J.M.; Zhu, X.B.; Sun, Y.P. Glucose-Induced Synthesis of 1T-MoS$_2$/C Hybrid for High-Rate Lithium-Ion Batteries. *Small* **2019**, *15*, 05420. [CrossRef]

46. Huang, M.J.; Chen, H.H.; He, J.; An, B.H.; Sun, L.N.; Li, Y.L.; Ren, X.Z.; Deng, L.B.; Zhang, P.X. Ultra small few layer MoS$_2$ embedded into three-dimensional macro-micro-mesoporous carbon as a high performance lithium ion batteries anode with superior lithium storage capacity. *Electrochim. Acta* **2019**, *317*, 638–647. [CrossRef]

47. Lin, J.; Shi, Y.H.; Li, Y.F.; Wu, X.L.; Zhang, J.P.; Xie, H.M.; Sun, H.Z. Confined MoS$_2$ growth in a unique composite matrix for ultra-stable and high-rate lithium/sodium-ion anodes. *Chem. Eng. J.* **2022**, *428*, 131103. [CrossRef]

48. Wang, X.L.; Li, G.; Seo, M.H.; Hassan, F.M.; Hoque, M.A.; Chen, Z.W. Sulfur Atoms Bridging Few-Layered MoS$_2$ with S-Doped Graphene Enable Highly Robust Anode for Lithium-Ion Batteries. *Adv. Energy Mater.* **2015**, *5*, 1501106. [CrossRef]

49. Wu, H.Y.; Zhang, X.E.; Wu, Q.H.; Han, Y.; Wu, X.Y.; Ji, P.L.; Zhou, M.; Diao, G.W.; Chen, M. Confined growth of 2D MoS$_2$ nanosheets in N-doped pearl necklace-like structured carbon nanofibers with boosted lithium and sodium storage performance. *Chem. Commun.* **2020**, *56*, 141–144. [CrossRef]

50. Zhang, S.; Zeng, Y.W.; Wang, Z.T.; Zhao, J.; Dong, G.D. Glycerol-controlled synthesis of MoS$_2$ hierarchical architectures with well-tailored subunits and enhanced electrochemical performance for lithium ion batteries. *Chem. Eng. J.* **2018**, *334*, 487–496. [CrossRef]

51. Cao, Y.P.; Chen, H.; Shen, Y.P.; Chen, M.; Zhang, Y.L.; Zhang, L.Y.; Wang, Q.; Guo, S.J.; Yang, H. SnS$_2$ Nanosheets Anchored on Nitrogen and Sulfur Co-Doped MXene Sheets for High-Performance Potassium-Ion Batteries. *ACS Appl. Mater. Interfaces* **2021**, *13*, 17668–17676. [CrossRef] [PubMed]

52. Cao, J.M.; Sun, Z.Q.; Li, J.Z.; Zhu, Y.K.; Yuan, Z.Y.; Zhang, Y.M.; Li, D.D.; Wang, L.L.; Han, W. Microbe-Assisted Assembly of Ti$_3$C$_2$T$_x$ MXene on Fungi-Derived Nanoribbon Heterostructures for Ultrastable Sodium and Potassium Ion Storage. *ACS Nano* **2021**, *15*, 3423–3433. [CrossRef] [PubMed]

53. Shi, M.J.; Wang, B.; Chen, C.; Lang, J.W.; Yan, C.; Yan, X.B. 3D high-density MXene@MnO$_2$ microflowers for advanced aqueous zinc-ion batteries. *J. Mater. Chem. A* **2020**, *8*, 24635–24644. [CrossRef]

54. Zhu, X.D.; Cao, Z.Y.; Wang, W.J.; Li, H.J.; Dong, J.C.; Gao, S.P.; Xu, D.X.; Li, L.; Shen, J.F.; Ye, M.X. Superior-Performance Aqueous Zinc-Ion Batteries Based on the In Situ Growth of MnO$_2$ Nanosheets on V$_2$CT$_x$ MXene. *ACS Nano* **2021**, *15*, 2971–2983. [CrossRef] [PubMed]